

## Neutral and charged photofragment coincidence imaging with soft x rays on molecular ion beams: Breakup of $\text{H}_3\text{O}^+$ at 13.5 nm

H. B. Pedersen,<sup>1,\*</sup> S. Altevogt,<sup>2</sup> B. Jordon-Thaden,<sup>2</sup> O. Heber,<sup>3</sup> L. Lammich,<sup>1</sup> M. L. Rappaport,<sup>3</sup> D. Schwalm,<sup>2</sup> J. Ullrich,<sup>2</sup> D. Zajfman,<sup>3</sup> R. Treusch,<sup>4</sup> N. Guerassimova,<sup>4</sup> M. Martins,<sup>5</sup> and A. Wolf<sup>2</sup>

<sup>1</sup>*Department of Physics and Astronomy, Aarhus University, DK-8000 Aarhus C, Denmark*

<sup>2</sup>*Max-Planck-Institut für Kernphysik, D-69117 Heidelberg, Germany*

<sup>3</sup>*Department of Particle Physics, Weizmann Institute of Science, Rehovot 76100, Israel*

<sup>4</sup>*HASYLAB at DESY, 22607 Hamburg, Germany*

<sup>5</sup>*Institut für Experimentalphysik, Universität Hamburg, D-22761 Hamburg, Germany*

(Received 16 March 2009; published 20 July 2009)

The fragmentation of the hydronium cation  $\text{H}_3\text{O}^+$  after photoabsorption at 13.5 nm has been investigated with a crossed-photon-and-ion-beams experiment making pulsing and trapping techniques available for fragment momentum imaging at the intense Free-electron LASer in Hamburg. The observed photofragmentation patterns demonstrate that the photolysis of  $\text{H}_3\text{O}^+$  proceeds by valence ionization into  $\text{H}_3\text{O}^{2+}$  which subsequently fragments to mainly  $\text{OH}+2\text{H}^+$  and  $\text{H}_2\text{O}^++\text{H}^+$  with a branching ratio of up to 0.6:1 and with different degrees of excitation of the molecular fragment. The cross section for fragmentation into  $\text{OH}+2\text{H}^+$  is found to be  $(0.37 \pm 0.18) \times 10^{-18} \text{ cm}^2$ , while the total photoabsorption cross section is estimated to be greater than  $0.95 \times 10^{-18} \text{ cm}^2$ . The data suggest that ionization mainly occurs from the  $3a_1$  and  $1e$  valence orbitals and that initial ionization from  $3a_1$  mainly leads to fragmentation into  $\text{H}_2\text{O}^+(A^2A_1)+\text{H}^+$  while initial ionization from the  $1e$  orbital predominantly populates the  $\text{H}_2\text{O}^+(B^2B_2)+\text{H}^+$  and  $\text{OH}(X^2\Pi)+2\text{H}^+$  channels. The results are of significance for astrophysical models of gas clouds in the vicinity of hot radiating objects and for models of the chemistry of planetary and lunar ionospheres under solar irradiation.

DOI: [10.1103/PhysRevA.80.012707](https://doi.org/10.1103/PhysRevA.80.012707)

PACS number(s): 34.80.Gs

### I. INTRODUCTION

The new free-electron laser (FEL) source Free-electron LASer (FLASH) at DESY in Hamburg [1,2] operates in the vacuum ultraviolet (vuv) to soft x-ray spectral region with pulse intensities exceeding any other existing light source in this regime by several orders of magnitude. With FLASH, experimental studies of fundamental processes using extremely dilute targets have become feasible in a new region of wavelength. This includes in particular the characterization of photofragmentation processes of molecular ions and radicals after valence shell excitation or ionization within a fast moving ion target.

Previously, we have reported results from a first crossed beams experiment where intense vuv pulses from FLASH were used to explore the photodissociation of the diatomic system  $\text{HeH}^+$  after electronic excitation [3]. In this paper we present results on the photofragmentation of the hydronium molecular ion  $\text{H}_3\text{O}^+$  at 13.5 nm (91.8 eV) where the breakup is initiated by ionization from the valence orbitals of the ion and we describe an improved experimental arrangement with fragment momentum resolving detectors for both light (e.g.,  $\text{H}$ ,  $\text{H}^+$ ,  $\text{H}_2$ , and  $\text{H}_2^+$ ) as well as for heavy neutral fragments (e.g.,  $\text{O}$ ,  $\text{OH}$ , and  $\text{H}_2\text{O}$ ).

The hydronium ion is of key importance for the chemistry of water in the liquid phase and it is a central species for the oxygen chemistry in a wealth of astrophysical environments [4,5] and in ionospheric regions of planetary atmospheres

[6]. In such environments, high energy radiation in the vuv to soft x-ray spectral region is frequently present, while on the other hand the photochemistry of the hydronium ion in this range is experimentally unexplored and its aspects are not included in present models beyond rough estimates.

In the electronic ground state, the nuclei of  $\text{H}_3\text{O}^+$  form a pyramidal geometry ( $C_{3v}$ ) around the central oxygen characterized by an opening angle of  $\angle\text{HOH} \sim 111.6^\circ$  and an OH bond length of  $\sim 1.84$  a.u. [7–10]. The electronic ground state of the ion is

$$(1a_1)^2(2a_1)^2(1e)^4(3a_1)^2X^1A_1, \quad (1)$$

where essentially  $1a_1$  and  $2a_1$  correspond to the oxygen  $1s$  and  $2s$  orbitals, the  $1e$  orbitals are located along the O-H bonds, and the  $3a_1$  orbital constitutes the lone pair. Upon absorption of a high energy photon ( $\gamma$ ),  $\text{H}_3\text{O}^+$  is further ionized by photoelectron emission from one of its energetically accessible valence orbitals in a vertical transition that preserves the nuclear conformation

$$\text{H}_3\text{O}^+(v,J) + \gamma \rightarrow \text{H}_3\text{O}^{2+}(v',J') + e^-. \quad (2)$$

Under these circumstances, the dication  $\text{H}_3\text{O}^{2+}$  is presumably formed in a repulsive state including significant vibrational excitation ( $v'$ ) and modified rotational excitation ( $J'$ ) depending on the angular momentum carried by the ejected photoelectron.

We report a characterization of the fragmentation of the  $\text{H}_3\text{O}^{2+}$  dication formed via photoionization at 91.8 eV showing that the fragmentation channels  $\text{H}_2\text{O}^++\text{H}^+$  and  $\text{OH}+2\text{H}^+$  are dominant although several other channels are energetically allowed. The results also indicate that the dication

\*Author to whom correspondence should be addressed; [hbp@phys.au.dk](mailto:hbp@phys.au.dk)

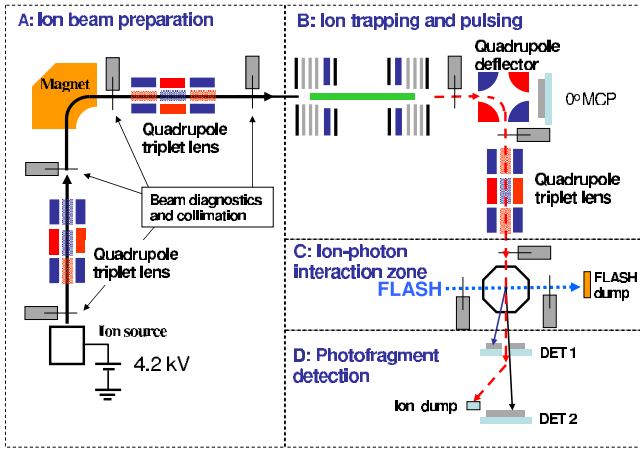


FIG. 1. (Color online) Scheme of the ion beam infrastructure Tiff installed at FLASH. The solid black line shows the dc ion beam, the thick green (light gray) line shows the optionally trapped beam, and the dashed red (gray) line shows the ion pulses behind the ion trap.

is mainly formed by ionization from the  $1e$  and  $3a_1$  orbitals among the three accessible ones at this photon energy and that the molecular fragments carry both electronic and vibrational excitations.

In Sec. II we give details on the experimental apparatus and the momentum imaging technique used to characterize the photofragments. The experimental findings are presented in Sec. III and the results are interpreted and discussed in Sec. IV.

**II. EXPERIMENT**

The experiment uses the ion infrastructure trapped ion fragmentation at an FEL (Tiff) installed at the free-electron laser facility FLASH at DESY, Hamburg, Germany. This arrangement combines fast beam photofragment imaging similar to previous developments [11,12] with the possibility of storing keV ion beams in an electrostatic trap [13] and the accelerator-based intense pulsed vuv and soft x-ray light source FLASH [1,2].

As illustrated in Fig. 1, a pulsed mass-selected monoenergetic ion beam at  $\sim 4.2$  keV kinetic energy is crossed at  $90^\circ$  with the FLASH laser pulses in an ion-photon interaction zone kept under ultrahigh-vacuum conditions. The electrical environment in the interaction zone is controllable both to allow for the variation in the ion energy at the point of photoabsorption and to enable the unique identification of mass and charge of the photofragments. The intensities of both the ion and photon beams are monitored together with their transverse spatial profiles at the interaction zone, while emerging photofragments are detected on two position and time sensitive detectors downstream from the interaction zone. Data are recorded from events where both ion and FLASH pulses are present simultaneously in the interaction zone (signal+background) interlaced with events where only ion pulses are present (background), allowing to deduce absolute reaction cross sections. With this imaging detection method the momenta of the emitted photofragments are de-

termined providing a characterization of the fragmentation pathways of the excited ion.

As indicated in Fig. 1, the complete ion beam infrastructure has four major functional regions, being (A) ion beam preparation, (B) ion trapping and pulsing, (C) ion-photon interaction, and (D) photofragment detection. Throughout the beamline, apart from the magnetic mass separation, the ion beam transport and focusing are achieved with electrostatic elements. The absolute ion beam current can be monitored at diagnostic stations located between the ion-optical elements, where the ion beam intensity and emittance can also be limited with insertable apertures and pairs of slits. In the following sections we describe in more detail the different functional regions of the beamline using  $H_3O^+$  as an example.

**A. Ion beam preparation**

The  $H_3O^+$  ions were produced in a hollow-cathode ion source of a design previously applied for cold  $H_3^+$  ion studies [11,14]. The source was biased to 4.2 kV in the present experiment and  $H_3O^+$  ions were obtained in a discharge supplied with pure water vapor. The pressure inside the source was typically  $\sim 0.05$  mbar and the discharge at 1050 V and 64 mA was sustained between two hollow electrodes of 10 mm inner diameter separated by 10 mm. A fast ion beam was extracted to ground potential through a 0.4 mm aperture in the vicinity of the negative glow of the hollow-cathode discharge. The kinetic energy  $E_0$  of the extracted ion beam depends both on the high voltage platform potential and on the potential of the plasma where the ions were created; for the present experiment this energy was determined in an independent measurement to be  $E_0 = 4245 \pm 10$  eV (see Sec. III A 1).

The extracted monoenergetic ion beam of typically a few  $\mu A$  was directed through a dipole sector magnet whereby the different mass components of the beam were analyzed. At the selected magnetic field a focused current of  $\sim 200$  nA of  $H_3O^+$  remained, while smaller currents of other water-related species, typically  $H_2O^+$  ( $\sim 150$  nA),  $OH^+$  ( $\sim 10$  nA), and  $O^+$  ( $\sim 3$  nA), were observed at nearby magnetic fields.

**B. Ion trapping and pulsing**

Figure 2 shows a schematic drawing of the linear ion beam trap integrated collinearly into the ion beamline. The purposes of this region are both trapping and pulsing of the mass-selected ion beam. The photofragmentation experiment requires a pulsed ion beam [3] to suppress background in the particle detectors. Moreover, storing the ions in a trap for time scales of milliseconds to seconds after production is beneficial to allow electronic and vibrational cooling of the initially excited ions emerging from the source; rotational cooling to room temperature is often also feasible [15,16].

The conceptual idea of the ion trap setup follows closely the design of the first described ion trap of this kind [13], consisting of two opposing electrostatic mirrors, each made of a stack of cylindrically symmetric electrodes. Each mirror has an inner part (electrodes 1–5 with voltages  $V_1$ – $V_5$  in Fig. 2) that is used to confine the ion beam longitudinally through an electrostatic barrier and an outer part (electrode 6 with

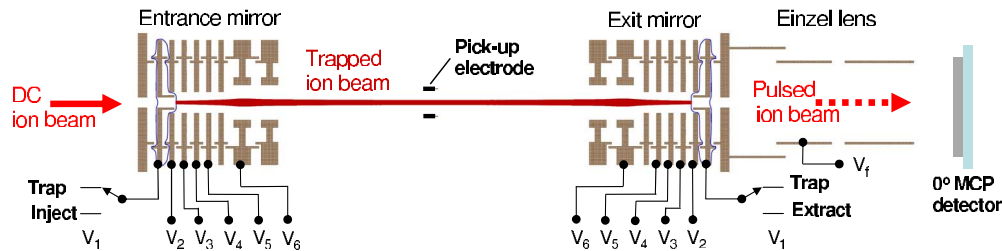


FIG. 2. (Color online) Schematic view of the electrostatic ion beam trap. The thin blue (black) line shows the electrostatic potential corresponding to the ion energy ( $E_0/qI$ ) in the trapping mode and the thick red (black) lines show trajectories of a 4.2 keV ion with the potential configuration  $\{V_1, V_2, V_3, V_4, V_5, V_6\} = \{4.8 \text{ kV}, 4.0 \text{ kV}, 3.0 \text{ kV}, 2.0 \text{ kV}, 1.0 \text{ kV}, 3.85 \text{ kV}\}$ .

voltage  $V_6$ ) that controls the focusing of the ion beam into the mirror. The electrical potential of this electrode determines largely the axial confinement of the ion beam in the trap and is selected such that trapping stability is ensured in analogy to an optical resonator [17,18].

A few major modifications have been made with respect to the original ion beam trap construction [13] to match the specific experimental conditions at the FLASH. The outermost electrodes (at voltage  $V_1$ ) with short cylindrical protrusions pointing toward the trap center are unique to the present electrostatic mirrors and are used for ion injection and extraction from the ion trap. Injection of ions into the trap is done by initially setting electrode 1 on the entrance side to a potential low enough to allow ions to pass into the ion trap while all other electrode potentials are kept statically in a configuration for ion trapping. The entering ion beam is trapped by switching  $V_1$  rapidly (within  $\sim 30\text{--}50$  ns) to a higher level, making the mirror reflecting. The time required to switch the potential is significantly shorter than the revolution time in the trap of typically a few microseconds (depending on both ion energy and mass). The actual voltage  $V_1$  used during injection is adjusted to match the ion beam focus to the ion trap acceptance.

On the exit side of the ion trap the corresponding electrode 1 is used to rapidly extract short bunches of ions from a trapped ion beam. In this operation  $V_1$  is first kept at a high level suitable for ion trapping, then switched to a low level for a short time ( $0.5\text{--}1 \mu\text{s}$ ), thereby generating a hole in the mirror that allows a pulse of ions to exit the trap, and finally raised to the high level again, leaving the major part of the ion beam inside the trap. This extraction cycle can be repeated to extract multiple short pulses of ions and it is essential in combination with the FLASH light source that delivers photon pulses in trains of closely spaced ( $5 \mu\text{s}$ ) pulses (see Sec. II C 2).

The second modification to the original design is the addition of an Einzel lens (with voltage  $V_f$ ) and a set of steering elements (not shown) on the exit side of the ion trap that allows to optimize the focusing and transport of the extracted ion pulse.

During storage the ion beam is monitored in two ways. Ion bunches can be observed with an electrostatic pickup positioned in the center of the ion trap [19]. Neutral particles created in collisions with the residual gas and exiting the ion trap through the exit mirror can be registered with a multi-channel plate (MCP) detector located at  $0^\circ$  downstream from the exit mirror [19].

Optionally, the ion trap assembly can be used as a *direct transfer* pulsing facility where electrode 1 on the entrance side is kept at a low potential continuously while electrode 1 on the exit side is switched between high and low levels to generate direct pulses from the ion source. This particular option was applied during the actual measurements on  $\text{H}_3\text{O}^+$  mainly because of the limited time available at FLASH for the present experiment.

The performance of the ion trapping and pulsing facility is illustrated by the data presented in Fig. 3. The decay of the  $\text{H}_3\text{O}^+$  ion beam during trapping is shown in Fig. 3(a) as observed using the  $0^\circ$  detector to count neutral particles exiting the ion trap. The initial nonexponential decay is typical for this type of ion beam trap [18] and can be modified using somewhat different injection conditions since it is mainly due to an emittance mismatch between the ion beam and the trap. The longer storage lifetime of about 6 s is due to beam loss through residual gas collisions (neutralization and multiple scattering). In the present case the residual gas had a pressure of  $\sim 6 \times 10^{-10}$  mbar and was composed mostly of  $\text{H}_2$ .

Also shown in Fig. 3 are the intensities of the extracted pulses for the case of direct transfer from the ion source (b) and for the case of intermediate ion beam trapping (c), measured after transport to the ion-photon interaction region (Sec. II C) by guiding the pulses into a cup connected to a charge sensitive amplifier. In this example, the trap is seen to be empty after six extractions of  $1 \mu\text{s}$  pulses at a frequency of 100 kHz simulating the photon pulse structure from FLASH.

The efficiencies of trapping and extraction are deduced from Fig. 3(d) where the intensities of single extracted ion pulses after trapping are compared to those for direct transfer. The trapping efficiency is  $\sim 20\%$  and essentially constant over the 200 ms time interval displayed, in agreement with the much longer overall ion beam lifetime in the trap. The trapping efficiency measured in this way represents a lower limit since it also depends on the initial beam emittance, and in fact an efficiency of  $\sim 100\%$  could be expected with an ion beam completely matched to the emittance accepted by the ion trap.

### C. Ion-photon interaction

The ion beam and the FLASH photon pulses were made to cross at  $90^\circ$  inside an interaction region shown schematically in Fig. 4(a). The beam crossing angle of  $90^\circ$  was set up

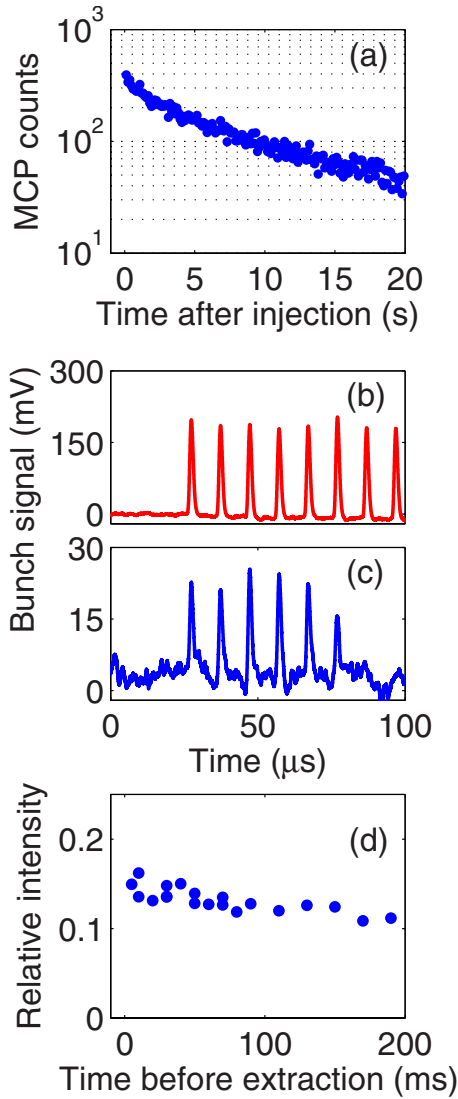


FIG. 3. (Color online) Trapping and pulsing of  $\text{H}_3\text{O}^+$  ions with the electrostatic ion beam trap. (a) Counts on the  $0^\circ$  MCP from neutral particles exiting the ion trap during trapping. At long times the decay is well represented by a single exponential function with a lifetime ( $1/e$ ) of 6.2 s. (b) Ion pulses observed on a metal cup for direct transfer through the ion trap to the interaction region. (c) Ion pulses for extraction of multiple pulses to the interaction region after 60 ms of trapping. (d) Intensity of a single extracted ion pulses relative to that of a directly transferred pulse.

to within  $0.3^\circ$  by passing the two beams through prealigned apertures on either side of the interaction region in the direction of both beams. The two beams cross in the middle of a central electrode with cylindrical bores of 10 mm in both the ion beam and the photon beam directions.

### 1. Ion beam and photofragments

Along the ion beam direction the interaction region has five 3-mm-thick electrodes on both the entrance and exit sides which all can be individually biased. The four outermost electrodes have an inner circular opening of 16 mm while the fifth electrode has an opening of 12 mm.

The electrical potential of the central electrode  $V_c$  determines the ion beam energy  $E_I$  at the moment of photoabsorption through  $E_I = E_0 - q_I V_c$ , where  $q_I$  is the ion charge and  $E_0$  is energy of the oncoming beam. The potentials on the entrance and exit sides can be used to affect the incoming ion beam and the outgoing ionic fragments. In fact, the electrode system can also be used as an ion trap similar to the one described in Sec. II B.

In the present experiment, the voltages on the electrodes along the ion beam direction were set as illustrated by the potential landscapes shown in Figs. 4(b) and 4(c). Here, the central electrode is biased at  $V_c = +75$  V which effectively lowers the ion energy at the point of interaction and served fragment identification by time-of-flight methods as described in Sec. II D 3, with only small transverse focusing effects. This potential on the central electrode is small ( $\sim 2\%$ ) relative to the original ion energy and no compensation of the beam focusing was needed for the incoming ion beam, i.e., all entrance electrodes were left at ground potential. On the exit side, the electrodes were biased for two purposes: to focus light outgoing fragments [ $\text{H}^+$  and  $\text{H}_2^+$ ; Fig. 4(b)] and to eliminate background from slow ions produced in the residual gas by the FLASH pulse [Fig. 4(c)]. With a positive potential on the central electrode, a slow positive ionic fragment resulting from photoionization of a residual gas molecule would be accelerated toward ground potential outside the interaction region and could give rise to an apparent FLASH-induced event on the particle detectors. Such events can be effectively suppressed by creating a reflecting electrostatic barrier slightly higher than the potential of the central electrode, as illustrated in Fig. 4(c), where the trajectory of a slow (2 eV) singly charged ion ( $\text{H}_2^+$ ) formed in the interaction region is shown. On the contrary, an ionic fragment of mass  $m_F$  originating from an ion of mass  $m_I$  in fast moving beam has a laboratory energy of  $\sim (m_F/m_I)E_I$  and is not reflected by the shallow electric barrier.

Immediately after the interaction zone, the ion beam can be bent into a metal cup where the ion intensity can be measured both as a current for a continuous beam and as a number of ions under pulsed operation. The equivalent (dc) ion beam current of the  $\text{H}_3\text{O}^+$  pulses let through to the interaction region was typically  $I_I = 60$  nA corresponding to a linear ion density of  $n_I = I_I / (v_I q_I) = 1.8 \times 10^3 \text{ mm}^{-1}$  in a pulse length of 1  $\mu\text{s}$ .

### 2. FLASH beam

In the present experiment the FLASH facility [1,2] was running at 5 Hz, delivering trains of 20 short ( $\sim 30$  fs) photon pulses at  $13.5 \pm 0.2$  nm separated by 5  $\mu\text{s}$  (200 kHz). The typical pulse energy was  $\sim 15$   $\mu\text{J}$  as determined from FLASH intensity monitors [20] corresponding to  $\sim 10^{12}$  photons per pulse. The pulse trains from FLASH were passed through the plane grating monochromator (PG2) beamline [21] operated with 1200 lines/mm grating in zeroth order to obtain a high transmitted photon flux and accepting the relatively large bandwidth of  $\pm 0.2$  nm. The estimated transmission of the PG2 beamline with our operating, including geometrical losses, was  $0.40 \pm 0.10$ . Thus, at the ion-photon interaction region, pulses of  $\sim (3-5) \times 10^{11}$  photons were de-

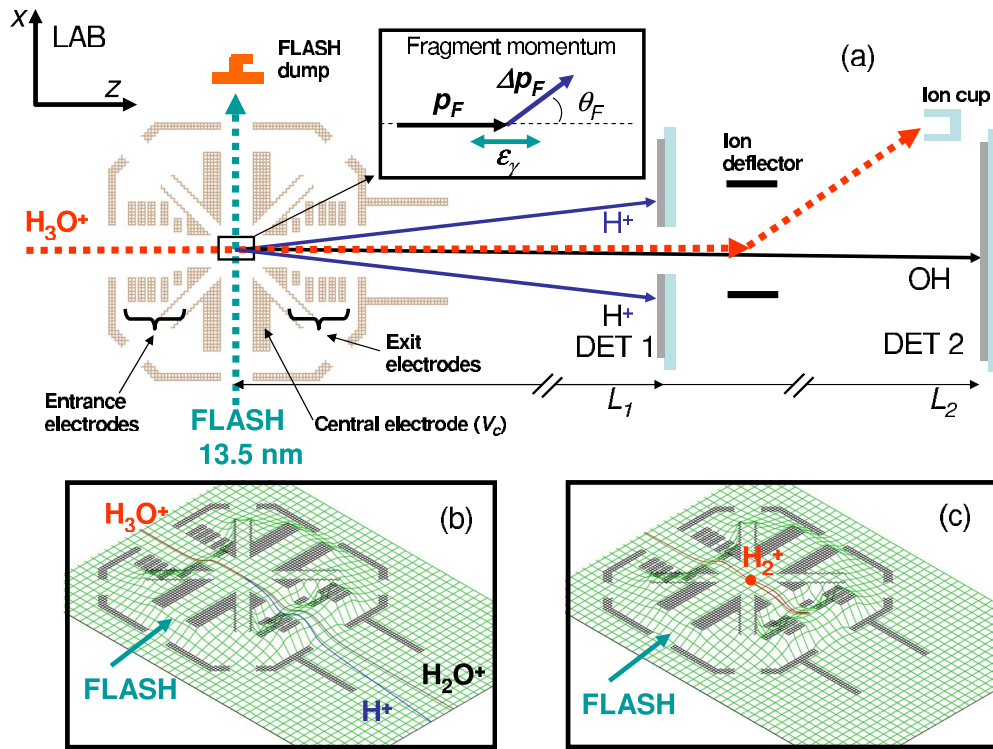


FIG. 4. (Color online) (a) The ion-photon interaction zone and fragment imaging system (not to scale) indicating the detection of the fragmentation channel  $\text{OH}+2\text{H}^+$ . The inset shows the fragment momentum representation as used in this paper with  $\epsilon_\gamma$  being the photon polarization (see Sec. II D 3). (b) Electrical potential surface in the interaction region and related ion trajectories for outgoing fragments after an  $\text{H}_3\text{O}^+$  breakup into  $\text{H}_2\text{O}^++\text{H}^+$  with a total kinetic energy release of 5 eV. (c) The same potential surface demonstrating the rejection of a slow (2 eV)  $\text{H}_2^+$  produced by FLASH in the residual gas [red (gray) dot].

livered with polarization parallel to the ion beam (horizontal). The results presented in this paper were obtained during 12 h of FLASH beam delivery including about 4 h of photon beam guiding through the PG2 beamline.

The FLASH beam, with a typical diameter of 1.5 mm at the TIFF interaction region, was aligned through and partly collimated by two 3 mm diameter apertures located about 0.5 m from either side of the interaction zone. Additional shields were installed on both sides of the interaction region to prevent stray photons from reaching the particle detectors. After the interaction region, the FLASH beam was dumped on a negatively biased ( $-800$  V) Cu structure, from which a photoelectric signal related to the FLASH intensity was recorded.

### 3. Ion-photon crossing

From each FLASH train, eight photon pulses were matched in time by ion pulses using the direct transfer mode of operation, giving an effective interaction rate of 40 Hz. To enable subtraction of background, parallel recordings with only a train of ions in the interaction region were interlaced between the trains of FLASH pulses.

During short breaks of the measurement, the interaction region was vertically displaced [ $y$  direction in Fig. 4(a)] and replaced by a diagnostics station for the two crossing beams. The intensity profiles of the two beams perpendicular to the crossing plane were recorded by moving a 1-mm-wide slit positioned at  $45^\circ$  relative to both beams vertically across the

interaction zone and recording the transmitted intensities immediately behind the slit. During this measurement the continuous (dc) ion beam current was recorded with an ammeter while the relative laser pulse intensity was monitored from the charge release from a negatively biased plate of stainless steel positioned behind the slit.

The measured beam profiles  $G_b$  ( $b=I, \gamma$  for ions and photons, respectively) can be described as

$$G_b(y) = \int g_b(y')s(y-y')dy', \quad (3)$$

where  $g_b(y')$  represents the actual beam profiles and  $s(y')$  represents the rectangular transmission function of the movable slit. The beam overlap is defined as

$$F = \int g_I(y)g_\gamma(y)dy. \quad (4)$$

The measured profiles of both the  $\text{H}_3\text{O}^+$  ion beam and the 13.5 nm photon pulses were well represented by Gaussian functions and after deconvolution  $F$  was determined to be  $F=5.5 \pm 1.0 \text{ cm}^{-1}$ .

### D. Fragment detection

The geometrical arrangement of the fragment detectors is illustrated in Fig. 4(a) with two 80 mm outer diameter position and time sensitive detectors oriented perpendicular to

the ion beam direction and located at  $L_1=263.0$  mm and  $L_2=872.1$  mm downstream from the interaction zone. With the first detector (DET 1), located at  $L_1$ , low-mass and energetic fragments are detected: in the present experiment, for instance, H,  $H^+$ ,  $H_2$ , and  $H_2^+$ . The detector has a central 20 mm diameter hole through which the ion beam and heavy fragments, as well as light fragments of low transverse momentum, pass, while fragments that separate sufficiently from the ion beam impinge on the surface of this detector. With the second detector (DET 2), located at  $L_2$ , neutral fragments are detected, while the ion beam and remaining charged fragments are directed into an ion beam cup.

**1. Mechanical and functional setup**

The detector for light fragments (DET 1) was developed in collaboration with RoentDek [22]; its mechanical construction is schematically shown in Fig. 5(a). The detector is composed of an MCP stack in chevron configuration equipped with a specially designed delay-line anode with three layers of delay lines arranged at  $60^\circ$  relative angles around the central hole. The outer radius of the active area of the detector is  $r_D=40$  mm and the radius of the hole is  $r_H=10$  mm. To ensure that the ion beam and the ionic fragments move in a field-free environment toward DET 1, a grounded mesh is located in front of the detector surface and the whole assembly is mounted on a grounded base plate facing the interaction region. To ensure that the passing ion beam and fragments are moving in a field-free region, a thin insulating tube with a grounded metallic layer on the inside is positioned in the central hole and extends on the rear side of the detector into a longer grounded metallic cylinder of larger diameter. The central hole through the detector also affects the electric field on the rear side of the MCP stack where a cloud of low energy electrons emerges in response to a particle impact on the detector front. To avoid curved electron trajectories between the rear side of the MCP stack and the delay-line anode, which would lead to nonlinearities in the imaging performance of the detector, the insulating tube was covered with a conducting layer on the outside extending from the rear of the MCP stack through the delay-line anode structure. By applying an electrical bias  $V_T$  to this layer the emerging electron showers from the rear side of the MCP stack move on approximately straight trajectories, as illustrated in the two insets of Fig. 5(b), showing the comparison of electron trajectories with and without the compensating bias.

The so-called hexanode structure of delay lines shown in Fig. 5(c) is used here to cover a large area of the circular detector with a central hole rather than to optimize the dead time properties of delay-line detectors [23]. At least two delay-line layers ( $u$ ,  $v$ , or  $w$ ) of the anode have to be activated by the impacting particle to determine the position of the impact, and thus this arrangement of three delay lines at  $60^\circ$  around the central hole does not allow imaging detection in a starlike pattern around the hole where only one layer of delay lines covers the area of the MCP (see Sec. II D 4).

The neutral particle detector, DET 2, consists of standard 80 mm (also  $r_D=40$  mm) MCPs in chevron configuration with a two layer delay-line anode arranged at  $90^\circ$  relative

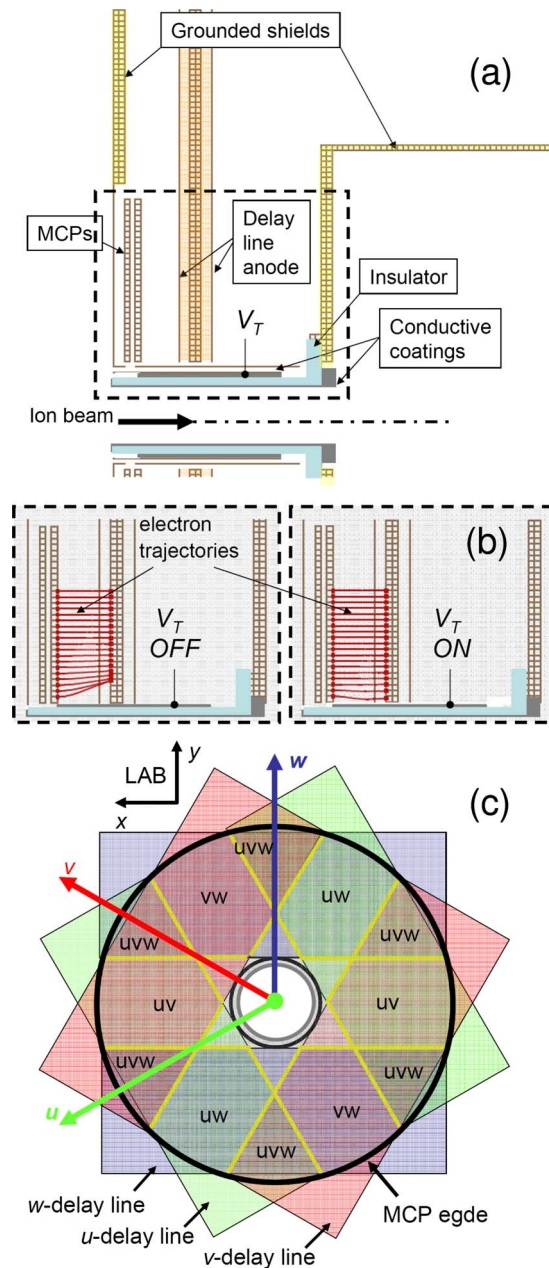


FIG. 5. (Color online) The new detector (DET 1) for light particle detection. (a) Schematic cut of the upper half showing the surrounding of the MCPs. (b) Trajectories [red (black) lines] of electrons exiting the rear of the MCP stack and impacting on the delay-line anode in the absence ( $V_T$  off) and presence ( $V_T$  on) of a compensating potential on the outer conductive coating of the central insulating tube. (c) Definition of hexagonal coordinates  $u$ ,  $v$ , and  $w$  and illustration of their relation to the hexanode delay lines. The coverage of the active MCP area (surrounded by the thick black line) by the different delay-line layers is indicated with the symbols  $uv$ ,  $uvw$ , etc.

angle [24]. To keep the surrounding chamber field free, this detector also has a grounded mesh in front of its surface.

The detection method based on the delay-line anode technology was adapted in the present setup because it allows precise and independent position and time information of impacting particles to be obtained at an acquisition rate

matched to the particular FLASH pulse structure. The electronic pulses generated on the delay lines of either detector as well as the pulses from one of the MCP faces (front or rear) were amplified and passed to constant fraction discriminator stages providing logic pulses with good time resolution; the logic pulses were fed to a time-to-digital converter with high resolution (25 ps). With this technique, nonlinear imaging performance of the detectors is still seen (and corrected for) around the central hole and near the outer detector rim since the shapes of the electronic pulses generated on the edges of a delay-line wire plane are different from those in its middle position.

## 2. Time and position detection and calibration

For an event  $i$  from a particle hitting on a detector (DET 1 or DET 2), the impact time  $T_d(i)$  is recorded from the pulse generated on either one of the faces of the MCP stack. The corresponding hit on the delay line  $k$  ( $k=u, v$ , or  $w$  for DET 1 and  $k=x, y$  for DET 2) generates electrical pulses traveling in both directions on the delay-line wire and arriving at the wire ends at times  $T_{k,1}(i)$  and  $T_{k,2}(i)$ , respectively. The so-called time sum  $\Sigma_k(i) = T_{k,1}(i) + T_{k,2}(i) - 2T_d(i)$  (with  $\Sigma_k \sim 70\text{--}80$  ns for DET 1 and  $\Sigma_k \sim 60$  ns for DET 2) is a constant that depends only on the length of the delay line. However, due to small variations in the shape of the analog pulses generated on the delay lines depending on the position of impact, variations in a few ns are seen in the recorded time sums when using constant fraction stages to form the logical timing pulses.

The time difference  $\Delta_k(i) = T_{k,1}(i) - T_{k,2}(i)$  contains the information on the position  $\delta_k(i)$  of impact on the axis defined by delay line  $k$ . For DET 2, which has two delay lines each covering the full MCP area, this relation can be written as

$$\delta_k(i) = \alpha_k[\Delta_k(i) + \beta_k] \quad (\text{DET } 2), \quad (5)$$

where  $\alpha_k \sim 0.5$  mm/ns and  $\beta_k$  (typically a fraction of a nanosecond) are experimentally determined parameters of calibration. The axes of the two delay layers of this anode form directly a Cartesian coordinate system, with the parameter  $\beta_k$  accounting for the offsets of the zero points from the geometrical crossing of the two axes. With the chosen orientation of the detector assembly this system coincides with vertical and horizontal axes in the laboratory, and the laboratory coordinates are obtained directly as  $x(i) = \delta_x(i)$  and  $y(i) = \delta_y(i)$ .

For DET 1, where each delay line covers two rectangular areas on both sides of the central hole [see Fig. 5(c)] the corresponding expression takes the form

$$\delta_k(i) = \alpha_k \times \begin{cases} [\Delta_k(i) + \beta_k^+], & \Delta_k(i) \geq 0 \\ [\Delta_k(i) - \beta_k^-], & \Delta_k(i) < 0 \end{cases} \quad (\text{DET } 1), \quad (6)$$

where  $\alpha_k \sim 0.3\text{--}0.4$  mm/ns and where the asymmetry introduced by the two values  $\beta_k^+$  and  $\beta_k^-$  (typically close to 20 ns) reflects the fact that the delay line is not perfectly symmetric around the central hole. The detector assembly is oriented such that one of the delay-line axes is collinear with the vertical laboratory axis while the two others form angles of

$60^\circ$  and  $120^\circ$  with respect to the vertical direction [see Fig. 5(c)].

A pair of coordinates  $\delta_\Gamma(i)$  with  $\Gamma = uv, uw$ , or  $vw$  [for instance,  $\delta_{uv}(i) = (\delta_u(i), \delta_v(i))$ ] obtained from either two of the three hexanode delay lines can be uniquely related to a set of coordinates in the laboratory frame when additionally the laboratory coordinates of the crossing point  $(x_\Gamma, y_\Gamma) \sim (0, 0)$  of the two hexanode axes are specified,

$$\begin{bmatrix} x(i) \\ y(i) \end{bmatrix} = \mathbf{R}_\Gamma \delta_\Gamma(i) + \begin{bmatrix} x_\Gamma \\ y_\Gamma \end{bmatrix} \quad (\text{DET } 1), \quad (7)$$

where the matrices  $\mathbf{R}_\Gamma$  contain the standard transformation from each of the hexagonal coordinate systems to the orthogonal one.

The calibration parameters for DET 1 [Eqs. (6) and (7)] and for DET 2 [Eq. (5)] were determined by recording single hits on each detector with masks of well known geometry located directly in front of the detectors. Thus, they were adjusted in a least-squares fitting routine such that the calculated distances between the holes in the mask matched the actual distance between the holes.

## 3. Fragment momentum determination

The inset of Fig. 4(a) shows the geometrical variables used to describe the photofragment momenta. To analyze a photofragmentation event we consider an ion of mass  $m_I$ , charge  $q_I$ , and initial kinetic energy  $E_0$  (before entering the biased region) undergoing photoabsorption in the interaction zone with the central electrode (see Sec. II C 1) biased to a potential  $V_c$ . At the moment of photoabsorption ( $t=0$ ) the laboratory momentum of the incident ion is  $p_I = \sqrt{2m_I(E_0 - q_IV_c)}$  and the ion beam is assumed to move along the laboratory  $z$  axis. After the photoabsorption the ion disintegrates promptly into photofragments, i.e., we neglect any motion of the fragmenting ion before its breakup.

In the center of mass (c.m.) frame of the ion, a photofragment of mass  $m_F$  and charge  $q_F$  is released with a momentum  $\Delta p_F$  in a direction characterized by the spherical angles  $\theta_F$  relative to the laser polarization  $\varepsilon_\gamma$  [Fig. 4(a)]. This c.m. momentum ( $\Delta p_F$ ) includes fractions of electronic, vibrational, and rotational energy released by the fragmenting molecular ion.

The laboratory momentum of a specific fragment  $F$  originating from the initial velocity ( $v_I$ ) of the molecular ion is  $p_F = m_F v_I = (m_F/m_I)p_I$ , giving rise to an overall forward motion. Hence, immediately after the breakup, the momenta of the fragment in the laboratory frame oriented parallel ( $\parallel$ ) and perpendicular ( $\perp$ ) to the initial ion beam direction are

$$\begin{aligned} p_F^\parallel &= \Delta p_F \cos(\theta_F) + p_F, \\ p_F^\perp &= \Delta p_F \sin(\theta_F). \end{aligned} \quad (8)$$

The released fragment then propagates through the electric fields in the interaction region, reaches the field-free flight region, and finally impacts on a detector positioned at a distance  $L$  ( $L_1$  or  $L_2$ ) from the interaction point at time  $t_F$  and radial displacement  $r_F$  from the ion beam axis. We define the generalized dimensionless coordinates,

$$\begin{aligned}\rho_F &= r_F/L, \\ \tau_F &= t_F/(L/v_i).\end{aligned}\quad (9)$$

The trajectory of the released fragment is obviously a function of the electric fields in the interaction region and the conversion of the measured coordinates  $\tau_F$  and  $\rho_F$  to c.m. parameters  $\Delta p_F$  and  $\theta_F$  requires, in general, numerical integration in the actual electric fields: thus, for the precise analysis of the results, the electric fields and fragment trajectories were modeled with the SIMION software [25].

To illustrate qualitatively the connection between properties of the fragment trajectories and experimental observables we consider two limiting cases where analytic expressions can easily be derived. First, when the interaction region is kept at ground potential ( $V_c=0$ ) or the released fragments are neutral, the momentum of a fragment is related to the measurable coordinates by  $\rho_F/\tau_F=p_F^\perp/p_F$  and  $1/\tau_F=p_F^\parallel/p_F$ , whereby the relative momentum is obtained as

$$\left[\frac{\Delta p_F}{p_F}\right]^2 = \left[\frac{\rho_F}{\tau_F}\right]^2 + \left[\frac{1}{\tau_F} - 1\right]^2 \quad (V_c=0) \quad (10)$$

and the c.m. angle of emission is given by

$$\tan(\theta_F) = \left[\frac{\rho_F}{\tau_F}\right] / \left[\frac{1}{\tau_F} - 1\right] \quad (V_c=0). \quad (11)$$

In another limiting case, the interaction region is approximated to be infinitely short, i.e., the fragments are assumed to be accelerated from the potential of the central electrode  $V_c$  to ground potential after the photofragmentation over a vanishing acceleration distance  $\Delta l_z$ . For this case, labeled as  $\Delta l_z=0$ , we obtain  $(1/\tau_F)^2 = (p^\parallel/p_F)^2 + \eta_F$ , where  $\eta_F = 2q_F m_F V_c / p_F^2 = (q_F/m_F)(m_i V_c / E_i)$ , and consequently the relations between the c.m. coordinates of a fragment and the observables  $(\rho_F, \tau_F)$  are

$$\left[\frac{\Delta p_F}{p_F}\right]^2 = \left[\frac{\rho_F}{\tau_F}\right]^2 + \left[\sqrt{\left[\frac{1}{\tau_F}\right]^2 - \eta_F} - 1\right]^2 \quad (\Delta l_z=0) \quad (12)$$

and

$$\tan(\theta_F) = \left[\frac{\rho_F}{\tau_F}\right] / \left[\sqrt{\left[\frac{1}{\tau_F}\right]^2 - \eta_F} - 1\right] \quad (\Delta l_z=0). \quad (13)$$

These equations illustrate how the potential  $V_c$  at the central electrode, i.e., the potential on which the photofragments are created, has a significant effect on the correlation of the observables  $\rho_F/\tau_F$  and  $1/\tau_F$  that depends uniquely on the fragment mass-to-charge ratio  $m_F/q_F$  through  $\eta_F$ . Thus, for a fixed value of  $\Delta p_F$ , Eq. (12) shows that the observables  $\rho_F/\tau_F$  and  $1/\tau_F$  will be confined on a half circle of radius  $\Delta p_F/p_F$  and centered at  $(\rho_F/\tau_F, 1/\tau_F) = (0, \sqrt{1+\eta_F})$ .

Finally, it should be emphasized that for a breakup into two fragments only, energy and momentum conservation ensures a correlation of  $(\rho_F/\tau_F)$  and  $1/\tau_F$  on a half circle with a distinct radius given by

$$\left(\frac{\Delta p_F}{p_F}\right)^2 = \frac{2\mu E_k}{p_F^2} \quad (\text{two body}), \quad (14)$$

where  $\mu$  is the reduced mass of the two body system and  $E_k$  is the total c.m. kinetic energy release.

#### 4. Geometric detector efficiency

The choice of the detector setup as shown in Fig. 4 and in particular the coverage of the active MCP area of DET 1 by the hexagonal delay-line structure displayed in Fig. 5(c) inhibits geometrically the detection of a part of the released photofragments. Light or energetic fragments can be lost from detection by impacting outside the active detector areas. Additionally, for DET 1 particles that pass through the central hole or hit inside the star-shaped region only covered by one delay-line layer will not be registered with full time and position information.

In analogy to the dimensionless coordinates in Eq. (9), we define the parameters  $\rho_D=r_D/L$  and  $\rho_H=r_H/L$  for the outer radius of the active MCP area and for the radius of the central hole, respectively. Evidently, fragments that impact on the detector at  $\rho_F > \rho_D$  or at  $\rho_F \leq 2\rho_H/\sqrt{3}$  are completely lost for detection. Additionally, for DET 2 a small part of the outer rimp is not accessible due to the blocking by DET 1. In the region  $2\rho_H/\sqrt{3} < \rho_F \leq 2\rho_H$  where the MCP is only partly covered by two delay-line layers, an impacting fragment is lost from detection with a probability proportional to the angular range covered by one delay line only [the star-shaped region around the central hole as seen Fig. 5(c)]. For a given  $\rho_F$ , this angular range can be expressed as  $\Delta\phi(\rho_F) = 12 \arccos[\rho_H/(2\rho_F) + \sqrt{3}/2\sqrt{1-(\rho_H/\rho_F)^2}]$ , and, in total, we define a detector acceptance function as

$$A_d(\rho_F) = \begin{cases} 0, & \rho_F \leq 2\rho_H/\sqrt{3} \\ 1 - \Delta\phi(\rho_F)/2\pi, & 2\rho_H/\sqrt{3} < \rho_F \leq 2\rho_H \\ 1, & 2\rho_H < \rho_F \leq \rho_D \\ 0, & \rho_F > \rho_D, \end{cases} \quad (15)$$

where  $(\rho_H, \rho_D) = (0.038, 0.150)$  for DET 1 and  $(\rho_H, \rho_D) = (0, 0.038)$  for DET 2. For a photoabsorption process, the angular distribution of emerging photofragments relative to the laser polarization (parallel to the laboratory  $z$  axis) can be characterized by the anisotropy parameter  $\beta$  through the relation [26]

$$F_\beta(\theta_F) d\theta_F = (1/2)[1 + \beta P_2(\cos(\theta_F))] d[\cos(\theta_F)], \quad (16)$$

where  $P_2$  is the second-order Legendre polynomial. Hence, for a given type of photofragment, characterized by the relative momentum release  $\Delta p_F/p_F$ , the geometric efficiency, i.e., total probability for the particle to impact on the active part of the detector, is

$$G_\beta\left(\frac{\Delta p_F}{p_F}\right) = \int A_d(\rho_F) F_\beta[\cos(\theta_F)] \left| \frac{d\cos(\theta_F)}{d\rho_F} \right| d\rho_F. \quad (17)$$

The explicit form of this distribution depends on the exact trajectories of the fragments from the interaction point to the

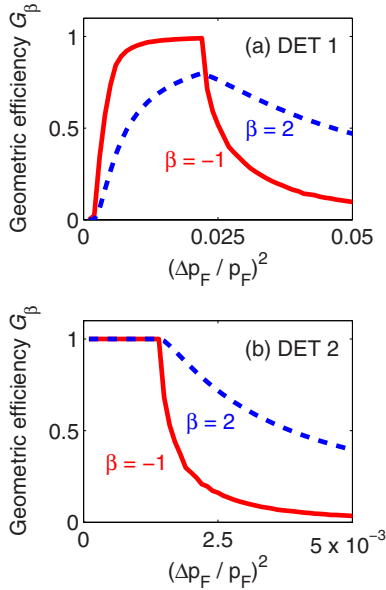


FIG. 6. (Color online) Geometric efficiencies as defined in Eq. (17) for (a) DET 1 and (b) DET 2 under field-free conditions,  $V_c = 0$ , i.e., using Eq. (18). The curves show the geometric efficiency for anisotropy parameter  $\beta = 2$  (dashed blue) and  $\beta = -1$  (solid red). The kinetic energy of the fragment can be obtained from  $E_F = E_I(m_F/m_I)(\Delta p_F/p_F)^2$ .

detectors, i.e., on the exact electrode potentials in the interaction region, and it is in general obtained through numerical simulation. If the interaction region is at ground potential,  $V_c = 0$ , valid for the main data sets presented in this work,  $G_\beta$  can be calculated analytically since in this case

$$\cos(\theta_F) = \frac{-\rho_F^2 \pm \sqrt{\left(\frac{\Delta p_F}{p_F}\right)^2 (1 + \rho_F^2) - \rho_F^2}}{\left(\frac{\Delta p_F}{p_F}\right)(1 + \rho_F^2)}, \quad (18)$$

where the equation is valid with plus and minus signs for  $\rho_F \leq \rho_0$  and  $\rho_F > \rho_0$ , respectively, with  $\rho_0 = (\Delta p_F/p_F)/\sqrt{1 - (\Delta p_F/p_F)^2}$ . Figure 6 shows the geometric efficiency for both DET 1 and DET 2 as a function of the relative fragment momentum release for  $\beta = -1$  and  $\beta = 2$ , representing the two limiting cases where the fragment is emitted preferentially perpendicular and parallel to the laser polarization, respectively.

### III. RESULTS

#### A. Data analysis

##### 1. Individual events

In the first step of the data analysis the events recorded with each detector (DET 1 or DET 2) were considered separately. The correspondence between signals recorded from an MCP face (front or rear, see Sec. II D 1) and signals from the delay lines was identified by requiring consistency with the known time sum  $\Sigma_k$  and time difference  $\Delta_k$  for the particular delay line.

Stray photons from the intense FLASH pulses occasionally generated hits on either detector that formed narrow well-separated peaks in the time-of-flight distributions mimicking the FLASH pulse structure. The precise arrival times  $T_\gamma$  of each of the eight used FLASH pulses in a pulse train were determined by analyzing these events from stray photons on both detectors and correcting for the photon time of flight to the detectors, i.e.,  $L_1/c \sim 0.88$  ns for DET 1 and  $L_2/c \sim 2.91$  ns for DET 2.

Each true fragmentation event  $i$  was then associated with a corresponding value for the FLASH pulse time, and the time of flight to the detector was determined as  $t_F(i) = T_d(i) - T_\gamma(i)$ . The impact positions  $[x_F(i), y_F(i)]$  on either DET 1 or DET 2 were determined from the time difference  $\Delta_k(i)$  according to the relations given in Sec. II D 2, i.e., in and around Eqs. (5)–(7).

The data were grouped in two parts according to whether the events were recorded with the FLASH pulses present (signal+background) or absent (background). The background origins mostly from fragmentation of ions in the residual gas; however, a smaller (15%) additional background is seen on DET 1 when the FLASH pulses are present arising from ions generated by the laser in the residual gas. By comparison between the time-of-flight distributions from these two groups, the FLASH-induced signal was clearly identified and the data set was reduced to include only events from these proper regions of time of flight. The mean position of photoabsorption events in the interaction region is reflected in a pair of coordinates  $(x_0, y_0)$  on each detector plane and the radial displacement of an event was calculated as  $r_F(i) = \sqrt{[x_F(i) - x_0]^2 + [y_F(i) - y_0]^2}$ . The values of the coordinates  $(x_0, y_0)$  were extracted from background subtracted projections on the horizontal and vertical axes, respectively.

The ion energy  $E_0$  was determined by considering the correlation between the measured mean time of flight  $\langle t_2 \rangle$  of neutral ( $q_F = 0$ ) fragments to DET 2 and the accurately known potential  $V_c$  at the interaction zone using the relation

$$\langle t_F \rangle = L_2 \sqrt{\frac{m_I}{2(E_0 - q_I V_c)}}. \quad (19)$$

With six recorded points for the potential  $V_c$  in the range of 0–400 V, the mean ion energy was determined to be  $E_0 = 4245 \pm 10$  eV from a least-squares fit to Eq. (19).

In the final step of the analysis of individual events, the reduced coordinates  $\rho_F(i)$  and  $\tau_F(i)$  and from those of the relative fragment momenta  $\Delta p_F(i)/p_F$  and angles  $\theta_F(i)$  were evaluated.

##### 2. Coincidence events

Within the samples of individual events on the two detectors grouped according to the FLASH pulses being present or absent, a search for coincidence hits originating from the same ion pulse was performed, both among events on a given detector and among events on both detectors. Figure 7 shows the map of coincidences between hits on the two detectors resulting from this analysis where also background subtraction has been performed.

It is evident that most (85%) of the hits on DET 1 are not coincident with hits on DET 2, and among the events on

		Hits on DET 1 (Light, charged or neutral)				SUM
		0	1	2	3	
Hits on DET 2 (Heavy, neutral)	0	X	4358	232	5	
	1	2003	738	53	1	2795
SUM			5096	285	6	

FIG. 7. (Color online) Photofragment coincidence map between photon induced hits on DET 1 and DET 2 as obtained without bias on the central electrode ( $V_c=0$ ).

DET 1 only, the majority (95%) are single hits with just a 5% contribution of double and much less triple hits. For the events where a neutral particle impacts on DET 2, about 70% are without coincidence on DET 1 while 27% and 2% have one and two coincidences, respectively. The search for coincidences among the events on DET 2 showed no contribution of double hits.

A complete analysis of the coincidence map shown in Fig. 7 evidently requires a detailed knowledge of the actual photofragmentation patterns and detector efficiencies ( $\varepsilon_1 \sim \varepsilon_2 \sim 50\%$ ). As illustrated in Fig. 6(a) a fraction of the fragments is lost for detection because of the central hole in DET 1: under the present conditions and with  $V_c=0$ ,  $H^+$  ions with kinetic energies of  $\leq 0.4$  eV and  $H_2^+$  with energies of  $\leq 0.8$  eV will, for instance, be completely lost from detection [ $G_\beta=0$  in Fig. 6(a)]. As a result of the deflection before DET 2, heavy charged fragments passing through the central hole in DET 1 will escape detection. Moreover, a fraction of light fragments will hit outside the active detector surface and will not be seen by any detector.

Despite these limitations at the present point of the argument, the coincidence map in Fig. 7 still demonstrates that the majority of the single hits on DET 1 do not have a heavy neutral partner. In consequence, the undetected fragments of these channels are charged and pass through the central hole in DET 1 where after they are deflected away before reaching DET 2 [see Fig. 4(a)]. We analyze these single photofragmentation events on DET 1 (total of 4358) in Sec. III B. Moreover, a substantial fraction of the neutral fragments detected with DET 2 (about 30%) is seen with one or two particles in coincidence on DET 1, and these events (total of 792) are investigated in more detail in Sec. III C.

### B. Light, charged, or neutral fragments

The direct correlation between  $\rho_F/\tau_F$  and  $1/\tau_F$  for the noncoincident events on DET 1 is shown in Fig. 8 both for a measurement with the interaction region kept at ground potential ( $V_c=0$ ) and for a measurement where the interaction region was biased to  $V_c=75$  V. The lines correspond to Monte Carlo trajectory simulations for  $H^+$  and  $H_2^+$  fragments with kinetic energy releases of 5 and 10 eV, respectively. It is evident that the majority of events in Fig. 8(a) form circular patterns which shift by the amount predicted for  $H^+$  rather

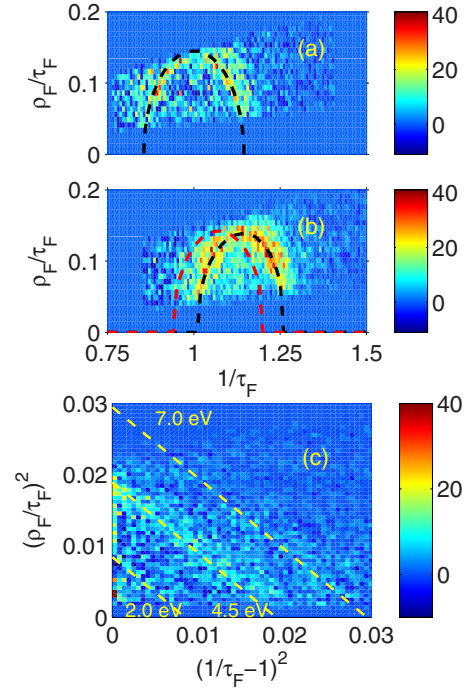
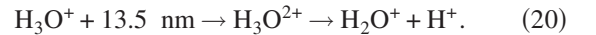


FIG. 8. (Color online) Momentum imaging of  $H_2O^+ + H^+$  from single (noncoincidence) events on DET 1 after background subtraction. (a) Correlation of  $\rho_F/\tau_F$  and  $1/\tau_F$  obtained with  $V_c=0$ . The dashed line shows the positions expected for  $H^+$  fragments released with a kinetic energy of 5 eV, as obtained from Monte Carlo trajectory simulations. (b) Same as (a) with  $V_c=75$  V. The dashed lines show the mean position for  $H^+$  (black) and  $H_2^+$  [red (gray)] fragments released with kinetic energies of 5 and 10 eV, respectively, as determined from ion trajectory simulations. (c) Linear correlation of  $(\rho_F/\tau_F)^2$  and  $(1/\tau_F)^2$  for  $V_c=0$  [cf. Eq. (10)].

than  $H_2^+$  when the interaction region is biased [Fig. 8(b)]. This becomes apparent when comparing the distribution in Fig. 8(b) to the predictions from the approximate formula given in Eq. (12), where an infinitely short interaction zone was assumed. For  $H^+$  fragments this equation predicts  $\eta_{H^+} = 0.333$  with a distribution centered around  $1/\tau_F = \sqrt{1 + \eta_{H^+}} = 1.155$ , while for  $H_2^+$  it predicts  $\eta_{H_2^+} = 0.167$  with a distribution centered at  $1/\tau_F = 1.080$ : the observed pattern in Fig. 8(b) is clearly consistent with the fragments being  $H^+$  rather than  $H_2^+$ .

The distinct correlations between  $(\rho_F/\tau_F)^2$  and  $(1/\tau_F)^2$ , displayed in Fig. 8(c) and visible as line-shaped features, identify the corresponding fragmentation to be a breakup into two particles with different energy releases  $(\Delta p_F/p_F)^2$  given by Eqs. (10) and (14). Hence, the majority of fragmentations observed with DET 1 result from the process



The coincidence map in Fig. 7 suggests that this is a strong channel as the single events on DET 1 represent the largest contribution.

The correlations shown in Fig. 8(c) can be further analyzed using Eqs. (10) and (14) to yield the kinetic energy release  $E_k$  for the events attributed to this channel. The cor-

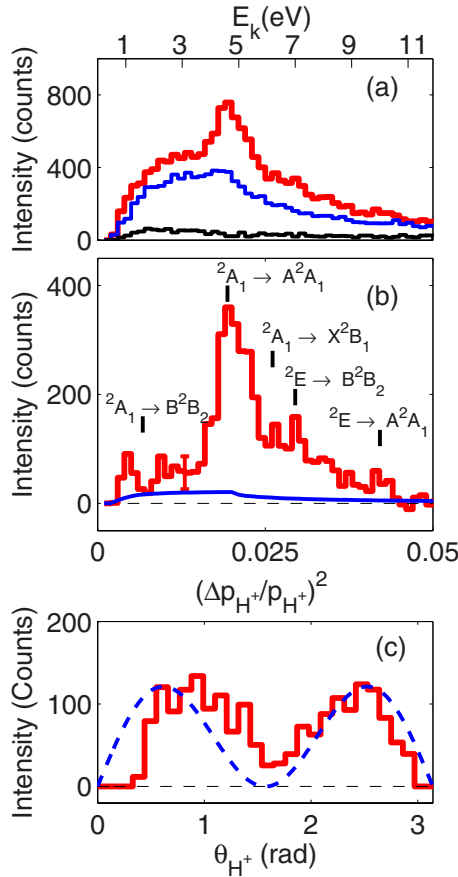


FIG. 9. (Color online) Fragmentation into  $\text{H}_2\text{O}^+ + \text{H}^+$  as observed with DET 1. (a) Relative momentum release of the  $\text{H}^+$  fragment and corresponding kinetic energy release  $E_k$  for events detected where both the FLASH and ions (red upper line), only ions (blue middle line), and only the FLASH (black lower line) were present in the interaction region. (b) Kinetic energy spectrum corrected for background. The spectrum has been tentatively assigned with transitions from  $\text{H}_3\text{O}_2^+$  ( $^2A_1$  and  $^2E$ ) to  $\text{H}_2\text{O}^+$  ( $X^2B_1$ ,  $A^2A_1$ , and  $B^2B_2$ ). A statistical error bar is given at  $(\Delta p_{\text{H}^+}/p_{\text{H}^+})^2 = 0.013$ . The blue lower line shows the expected contribution from the channel [Eq. (21)]; see Sec. III C. (b) Distribution of fragmentation angles  $\theta_{\text{H}^+}$  relative to the FLASH polarization ( $\epsilon_\gamma$ ) direction for  $4.0 \text{ eV} \leq E_k \leq 5.7 \text{ eV}$ . The dashed line (blue) shows a distribution corresponding to fragmentation preferentially along the laser polarization axis ( $\beta=2$ ).

responding spectra are displayed in Figs. 9(a) and 9(b), where in Fig. 9(a) the components of the background from ion fragmentation caused by collisions in the residual gas (blue middle line) and from ions generated by the FLASH in the residual gas (black upper line) are also shown. The resulting kinetic energy spectrum after background subtraction [Fig. 9(b)] exhibits smaller structures at low energies ( $\sim 1$  and  $\sim 2$  eV), a larger peak around 4.8 eV, and a broader pattern centered around 7 eV and extending up to  $\sim 10$  eV. The possible assignment of these structures to  $\text{H}_2\text{O}^+$  final states is indicated in the figure and will be discussed in Sec. IV A.

For the major peak at  $E_k = 4.0\text{--}5.7$  eV the distribution of fragment directions relative to the laser polarization is shown in Fig. 9(c) and it is seen that this breakup yields fragments

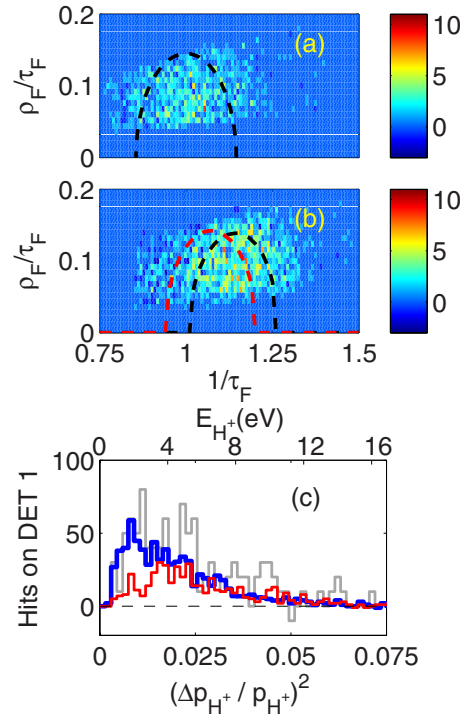


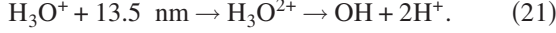
FIG. 10. (Color online) Momentum imaging for  $\text{OH} + 2\text{H}^+$  channel observed with DET 1 after background subtraction. (a) Correlation of  $\rho_F/\tau_F$  and  $1/\tau_F$  at  $V_c=0$  requiring one coincidence with DET 2 (total of 738). The dashed line shows the positions expected for  $\text{H}^+$  fragments released with a kinetic energy of 5 eV, as obtained from Monte Carlo trajectory simulations. (b) Same for  $V_c=75$  V (total of 1265). The dashed lines show the mean position for  $\text{H}^+$  (black) and  $\text{H}_2^+$  [red (gray)] fragments released with kinetic energies of 5 and 10 eV, respectively, from ion trajectory simulations. (c) Relative momentum release of  $\text{H}^+$  fragments at  $V_c=0$  requiring a coincidence with DET 2. The thick solid (blue) line shows the distribution observed when a single  $\text{H}^+$  was detected in coincidence (total of 738). The light gray line marks the distribution, amplified by a factor of 10, when two  $\text{H}^+$  fragments were detected in coincidence with a hit on DET 2 (total of  $2 \times 53$ ), and the red (gray) line displays the observed spectrum when two  $\text{H}^+$  particles were observed without a coincidence on DET 2 (total of  $2 \times 232$ ). The upper scale shows the corresponding kinetic energy of the  $\text{H}^+$  fragments,  $E_{\text{H}^+} = E_I(m_{\text{H}^+}/m_I)(\Delta p_{\text{H}^+}/p_{\text{H}^+})^2$ .

emitted preferentially along the laser polarization axis. We refrain from evaluating similar angular distributions for the events in other regions of kinetic energy release based on the present data because of limited statistics and the partial loss of the channels from detection for the lowest and highest energy releases.

### C. Coincidences with a heavy neutral fragment

Figures 10(a) and 10(b) present the  $(\rho_F/\tau_F)-(1/\tau_F)$  correlation for events recorded at DET 1 in coincidence with one neutral fragment on DET 2 for measurements with  $V_c=0$  and  $V_c=75$  V, respectively. The distributions are broad with the events scattered evenly over a rather wide area of the  $(\rho_F/\tau_F)-(1/\tau_F)$  plane showing explicitly that the breakup process associated with these fragments involves more than

two particles for this coincidence condition; a two body breakup process would have resulted in a distinct  $(\rho_F/\tau_F)-(1/\tau_F)$  correlation as seen from Eq. (14). By comparison to Monte Carlo trajectory simulations [or approximate formula (12)], the displacement of the observed distribution when applying 75 V bias to the central electrode identifies the fragments as  $H^+$  particles. In particular, it is evident that the distributions shown in Figs. 10(a) and 10(b) do not originate from neutral fragments ( $H$ ,  $H_2$ ). Based on these evidences, the process responsible for a large fraction of the observed fragmentation can be identified as



The detection of all three particles is obtained for about 2% (total of 53) of the events. A total efficiency for  $H^+$  detection on DET 1 of  $\sim 15\%$  is indicated by the coincidence map, and with an MCP efficiency of  $\varepsilon_1 \sim 50\%$  we find a geometric efficiency of  $G_\beta \sim 30\%$ . As rationalized below, the limited geometric efficiency [cf. Fig. 6(a)] probably originates from a large fraction of  $H^+$  ions with low energy. Due to this significant  $H^+$  loss and the limited statistics of triple coincidence events (total of 53) we refrain from a further analysis of the dynamics for the  $H^+$  fragments from the channel according to Eq. (21).

Beyond their occurrence where two (total of 738) or three (total of 53) particles are detected in coincidence on DET 1 and DET 2, the  $H^+$  fragments from the process in Eq. (21) should also contribute to the coincidence map for DET 1 without a coincidence on DET 2 both for single hits (total of 4358), and where two particles are detected in coincidence (total of 232). With an MCP efficiency of DET 2 of  $\varepsilon_2 \sim 50\%$  about 710 single events are thus expected on DET 1, and the corresponding contribution to the kinetic energy distribution for the channel in Eq. (20) is displayed as the blue lower line in Fig. 9(b) assuming an isotropic fragmentation [ $\beta=0$ , Eq. (16)] and a random energy sharing among the fragments.

For coincidence detection of two particles on DET 1, only some 50 of the 232 observed events are expected to originate from the process in Eq. (21). Figure 10(c) shows the relative momentum release and kinetic energy distribution of the  $H^+$  fragments from the three regions of the coincidence map where the process in Eq. (21) is expected to contribute. The distributions requiring coincident events with DET 2, i.e., the blue (gray) and light gray lines, have very similar shape, providing further evidence that these parts of the coincidence map indeed originate from the same process [Eq. (21)]. The spectrum for events where no coincidence is required on DET 2, i.e., the red line, has a different form, resembling the distribution shown in Fig. 9(a), which gives evidence that the major part of events with two hits on DET 1 (total of 232) results from random coincidences of  $H^+$  particles from the process  $H_2O^+ + H^+$  [Eq. (20)].

In Fig. 11(a) the observed  $(\rho_F/\tau_F)-(1/\tau_F)$  correlation is illustrated for the FLASH-induced OH hits on DET 2. These events occupy a relatively small area of the correlation diagram evidencing that they carry a large fraction of the original mass. Figure 11(b) shows the relative momentum release distributions for the observed OH fragments both with and

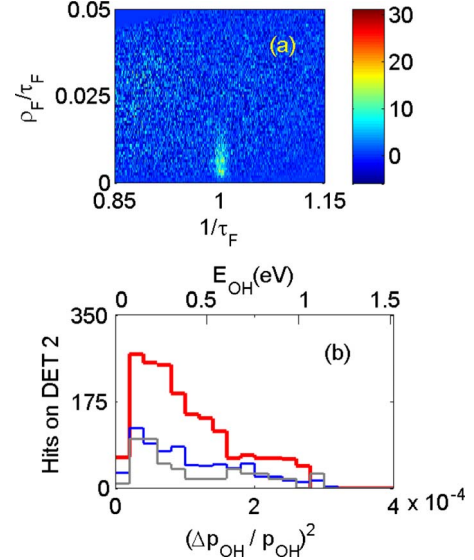


FIG. 11. (Color online) Momentum imaging of the  $OH+2H^+$  channel obtained with DET 2. (a) Correlation of  $\rho_F/\tau_F$  and  $1/\tau_F$ . (b) Relative momentum release of OH fragments requiring no coincidence on DET 1 (thick red line, 2003 events), requiring one  $H^+$  fragment in coincidence on DET 1 [thin blue (gray) line, 738 events], and the distribution, amplified by a factor of 10, when two  $H^+$  fragments were detected in coincidence on DET 1 (light gray line, total of  $2 \times 53$  entries). The upper scale shows the corresponding kinetic energy of the OH fragments,  $E_{OH} = E_I(m_{OH}/m_I)(\Delta p_{OH}/p_{OH})^2$ .

without coincidence hits on DET 1. The spectra have very similar shapes, being strongly peaked toward lower momentum releases. This observation, similar to the agreement of the blue (gray) and light gray lines in Fig. 10(c), is in complete consistency with the identification of Eq. (21) to be underlying breakup process.

#### D. Absolute cross section

Since all OH fragments impinge on DET 2, the absolute cross section for  $H_3O^+$  breaking up into  $OH+2H^+$  at 13.5 nm [Eq. (21)] can be estimated from the total counts of the OH products on this detector. The ion beam was found to be homogeneous in the longitudinal propagation direction as seen from the time independence of the neutral background count rate on DET 2. The longitudinal movement of the ion pulse during the passage of a FLASH pulse is  $\sim 5 \mu\text{m}$  and hence to a very good approximation, the ion pulse can be considered frozen during the irradiation. Based on these considerations, the absolute reaction cross section can be deduced as

$$\sigma_{OH+2H^+} = \frac{N_{OH}}{\varepsilon_2 F T_{PG2} \sum_{\gamma} \langle n_{\gamma} n_I \rangle} \approx \frac{N_{OH} \times q_I v_I}{\varepsilon_2 F T_{PG2} N_{\gamma} \langle n_{\gamma} \rangle \langle I_I \rangle}, \quad (22)$$

where  $N_{OH}$  represents the number of observed events and  $\varepsilon_2 = 0.5 \pm 0.1$  is the detector efficiency of DET 2. The sum extends over all performed temporal FEL-ion overlaps ( $N_{\gamma} = 3.52 \times 10^5$ ) in this measurement. The number of photons

per pulse  $n_\gamma$  was measured directly with the FLASH photon monitors [20] before the PG2 beamline and the intensity transmission through the PG2 beamline to the interaction point was  $T_{PG2}=0.40 \pm 0.10$ . The beams' overlap was determined to be  $F=5.5 \pm 1.0 \text{ cm}^{-1}$  (see Sec. II C 3). In total, the absolute cross section for this channel is determined to be

$$\sigma_{\text{OH}+2\text{H}^+} = (0.37 \pm 0.18) \times 10^{-18} \text{ cm}^2. \quad (23)$$

The error bars reflect several systematic uncertainties associated with the photon pulse intensity measurements both with respect to the direct determination of  $n_\gamma$  ( $\sim 15\%$ ) as well as the calculation of the beamline transmission  $T_{PG2}$  ( $\sim 25\%$ ) and the detector efficiency ( $\varepsilon_2$ ) ( $\sim 20\%$ ), while the statistical error from the detector counts amounts to about 6%.

The absolute cross section for  $\text{H}_3\text{O}^+$  breaking up into  $\text{H}_2\text{O}^+ + \text{H}^+$  as observed with DET 1 through the  $\text{H}^+$  fragment cannot be obtained directly from the counts on DET 1 since, owing to the lack of information on the angular dependence of the fragmentation [see Fig. 6(b)], an unknown fraction of the  $\text{H}^+$  particles is lost either through the central hole or outside the detector. From the coincidence map in Fig. 7 it is evident that this channel is more intense than the  $\text{OH} + 2\text{H}^+$  channel. In a conservative estimate, where we assume that all noncoincidence  $\text{H}^+$  fragments are, in fact, seen by the DET 1 and that the efficiencies of the two detectors are similar, we can derive a lower limit on the cross section of  $\sigma_{\text{H}_2\text{O}^+ + \text{H}^+} \geq (4358/2795) \times 0.37 \times 10^{-18} \text{ cm}^2 = 0.58 \times 10^{-18} \text{ cm}^2$  and a total photoabsorption cross section of  $\geq 0.95 \times 10^{-18} \text{ cm}^2$ .

For the fragmentation into the channel characterized by a kinetic energy release of  $4.0 \text{ eV} \leq E_k \leq 5.7 \text{ eV}$ , assigned to fragmentation via the  ${}^2\text{A}_1$  state of  $\text{H}_3\text{O}^{2+}$  into  $\text{H}_2\text{O}^+(A {}^2\text{A}_1) + \text{H}^+$ , the angular dependence is, in fact, known as shown in Fig. 9(c) and the geometric acceptance for this channel is  $G_{\beta=2} \sim 70\%$ . Hence, for this particular channel, the absolute cross section can be estimated to be  $(0.44 \pm 0.22) \times 10^{-18} \text{ cm}^2$ .

## IV. DISCUSSION

### A. Interpretation of fragmentation patterns

The absorption of a high energy photon by  $\text{H}_3\text{O}^+$  could lead either to electron *excitation* into a dissociating state of the monocation where the photon energy is shared between fragment excitation and kinetic energy release or to *ionization* into a fragmenting state of the dication where the photoelectron carries away a significant portion of the energy provided by the photon. On the time scale of the nuclear motions photoabsorption is prompt and the nuclei are essentially frozen during the process. For a photoexcitation process to be effective from the  $X {}^2\text{A}_1$  ground state of  $\text{H}_3\text{O}^+$ , excited quantum states of symmetry  ${}^2\text{A}_1$  or  ${}^2\text{E}$  need to be available at the ground state nuclear geometry in the photon energy region. In contrast, the conditions for an effective photoionization are much more relaxed since the outgoing photoelectron carries both energy, orbital angular momentum, and spin. Moreover, as the photon energy is above 90 eV in the present experiments the possible excited states will be far above the  $\text{H}_3\text{O}^+$  ionization limit and therefore are ex-

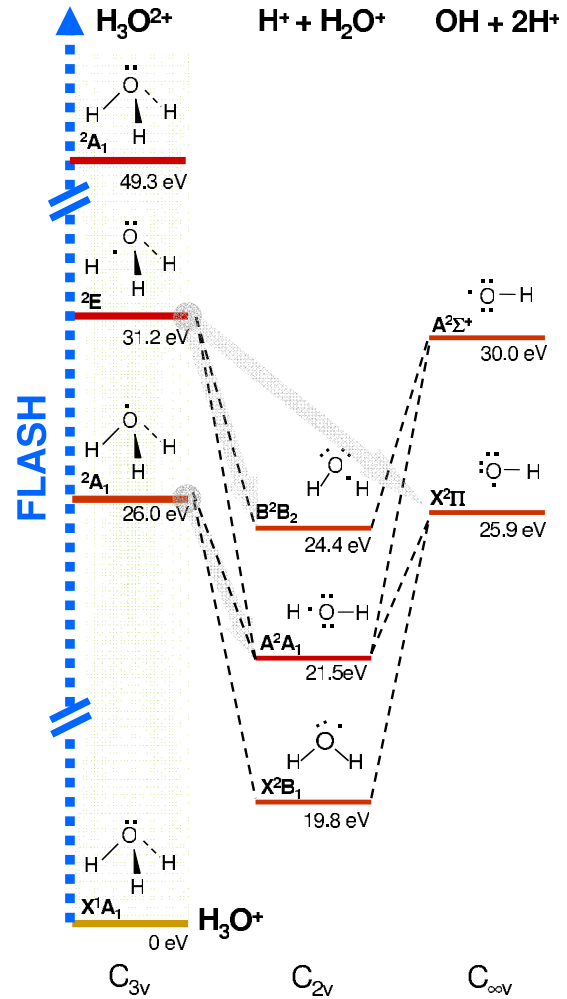


FIG. 12. (Color online) Schematic energy structure of lowest states of the  $\text{H}_3\text{O}^+$ ,  $\text{H}_3\text{O}^{2+}$ ,  $\text{H}_2\text{O}^+ + \text{H}^+$ , and  $\text{OH} + 2\text{H}^+$  systems. The gray arrows show the reaction pathways identified in the present study. The  $\text{H}_3\text{O}^{2+}$  energies were obtained as orbital energies of  $\text{H}_3\text{O}^+$  given in Ref. [27]. The energies in the fragmentation channels were calculated from data available at the NIST database [29], in particular the proton affinity of  $\text{H}_2\text{O}$  (7.2 eV), the ionization energy of  $\text{H}_2\text{O}$  (12.6 eV), the proton affinity of  $\text{OH}$  (6.1 eV), and the excited state energies of  $\text{H}_2\text{O}^+$  (1.7 and 4.6 eV) and  $\text{OH}$  (4.1 eV).

pected to show rapid autoionization in most cases. The observed channels ( $\text{H}_2\text{O}^+ + \text{H}^+$  and  $\text{OH} + 2\text{H}^+$ ) are consistent with nuclear breakup from the dication, i.e., the competing photoexcitation seems to be insignificant for  $\text{H}_3\text{O}^+$  at 13.5 nm.

At the present photon energy of 91.8 eV, photoelectric emission from  $\text{H}_3\text{O}^+$  is possible from the valence orbitals  $2a_1$ ,  $1e$ , or  $3a_1$ , with orbital binding energies of 49.3, 31.2, and 26.0 eV, respectively [27], which translate into equivalent excitation energies of the  $\text{H}_3\text{O}^{2+}$  product ion after the electron escape (Koopmans' theorem [28]), as illustrated schematically in Fig. 12. The threshold for two-electron ionization into  $\text{H}_3\text{O}^{3+}$  is found around 60 eV [27] and autoionization from transient  $\text{H}_3\text{O}^{2+}$  states is energetically forbidden for this relatively small molecular system. The experimentally observed fragmentation patterns are completely domi-

nated by the  $\text{H}_2\text{O}^+ + \text{H}^+$  and  $\text{OH} + 2\text{H}^+$  channels, whereas energetically the fragmentation of the formed  $\text{H}_3\text{O}^{2+}$  dication is allowed to proceed via into several other pathways.

Considering initial ionization of an electron from the  $3a_1$  orbital, leaving the  $\text{H}_3\text{O}^{2+}$  in the  ${}^2A_1$  state of about 26.0 eV above the hydronium ground state, fragmentation is allowed into  $\text{H}_2\text{O}^+ + \text{H}^+$  (19.8 eV and above),  $\text{OH}^+ + \text{H}_2^+$  (22.7 eV and above), and  $\text{OH} + 2\text{H}^+$  (25.9 eV and above). Fragmentation from this level into the unobserved  $\text{OH}^+ + \text{H}_2^+$  channel would be associated with a kinetic energy release of about 3.3 eV, which for the  $\text{H}_2^+$  fragments is equivalent to  $(\Delta p_F/p_F)^2 = 6.5 \times 10^{-3}$ . As seen from Fig. 6(a), depending on the fragmentation anisotropy, this would result in a geometric efficiency of DET 1 of 40%–80% that, combined with the MCP efficiency of  $\sim 50\%$ , results in a total observation efficiency for  $\text{H}_2^+$  from this channel of 20%–40%: from the absence of this channel in the experimental observation, it thus seems evident that  $\text{OH}^+ + \text{H}_2^+$  does not contribute significantly to the dissociation from the  ${}^2A_1$  state. The fragmentation into  $\text{OH} + 2\text{H}^+$  from the  ${}^2A_1$  of  $\text{H}_3\text{O}^{2+}$ , however, is associated with very low kinetic energy release ( $\sim 0.1$  eV) and  $\text{H}^+$  fragments from this decay channel escape detection on DET 1; the neutral OH would still be seen on DET 2. Hence, based on the present experiment, we cannot exclude a contribution from this channel to the breakup of the  ${}^2A_1$  state.

Through ionization from the  $1e$  orbital, the  $\text{H}_3\text{O}^{2+}$  dication is formed in the  ${}^2E$  state at 31.2 eV above the ground state of  $\text{H}_3\text{O}^+$  and again fragmentation from this level is energetically allowed into several channels beyond the observed  $\text{H}_2\text{O}^+ + \text{H}^+$  and  $\text{OH} + 2\text{H}^+$ . Two-body breakup into  $\text{OH}^+ + \text{H}_2^+$  (22.7 eV and above), occurring with a relatively high kinetic energy release ( $\leq 8.5$  eV), can be excluded as a significant fragmentation channel from the measurements with a biased interaction region since the majority of fragments observed on DET 1 were identified as  $\text{H}^+$ . Breakup into channels with relatively energetic neutral fragments of  $\text{H}_2$  or  $\text{H}$ , i.e.,  $\text{O}^+ + \text{H}^+ + \text{H}_2$  (26.1 eV,  $E_{\text{H}_2} \leq 5.1$  eV),  $\text{OH}^+ + \text{H}^+ + \text{H}$  (26.5 eV,  $E_{\text{H}} \leq 4.7$  eV), and  $\text{O}^+ + \text{H}_2^+ + \text{H}$  (27.9 eV,  $E_{\text{H}} \leq 3.3$  eV), can similarly be excluded as significant decay channels since corresponding neutral fragments were not distinguished on DET 1, as revealed by the measurements with a biased interaction region. Moreover, breakup into  $\text{O} + \text{H}^+ + \text{H}_2^+$  (27.9 eV,  $E_{\text{H}^+}$  and  $E_{\text{H}_2^+} \leq 3.3$  eV) also seems insignificant because the corresponding  $\text{H}_2^+$  was not identified on DET 1 despite a fair geometric acceptance for the relevant kinetic energies.

A complete breakup of the  $\text{H}_3\text{O}^{2+}$  dication into either  $\text{O}^+ + \text{H}^+ + 2\text{H}$  or  $\text{O} + 2\text{H}^+ + \text{H}$  (both with  $\sim 30.6$  eV, i.e.,  $E_{\text{H}} \leq 0.6$  eV) is also possible from the  ${}^2E$  state. For these channels light fragments ( $\text{H}$  or  $\text{H}^+$ ) would mostly escape detection on DET 1; however neutral fragments ( $\text{O}$  and/or  $\text{H}$ ) would be detected on DET 2, as for an oxygen fragment  $\Delta p_{\text{O}}/p_{\text{O}} \leq 0.013$  while for hydrogen  $\Delta p_{\text{H}}/p_{\text{H}} \leq 0.051$ . Since the measurements with DET 2 [Fig. 11(a)] showed no evidence for neutral hydrogen fragments consistent with these energies we concluded that they are insignificant in the photofragmentation of  $\text{H}_3\text{O}^+$ .

The experimental evidence in this study thus points to a dynamically (as opposed to statistically) dominated photoly-

sis of  $\text{H}_3\text{O}^+$  where only few of the energetically available fragmentation channels are significant. Since the observed fragmentation patterns are related to particular electronic states of the dication formed by nonresonant photoionization with a nuclear geometry given by the initial  $\text{H}_3\text{O}^+$  system, they can be expected to govern the process over a wide range of photon energies around the one applied here.

Figure 12 shows the energetic positions of the lowest states of the  $\text{H}_3\text{O}^{2+}$ ,  $\text{H}_2\text{O}^+ + \text{H}^+$ , and  $\text{OH} + 2\text{H}^+$  systems. Considering the kinetic energy releases as seen from this diagram the tentative assignment of the kinetic energy spectrum in Fig. 9(a) was made for the  $\text{H}_2\text{O}^+ + \text{H}^+$  channel. The data suggest that ionization from the  $3a_1$  and  $1e$  valence orbitals is most significant while no transitions from  $2a_1$  are needed to assign the observed spectrum. Initial ionization from  $3a_1$  leads mainly to fragmentation into  $\text{H}_2\text{O}^+(A {}^2A_1) + \text{H}^+$  with possible smaller fractions going to  $\text{H}_2\text{O}^+(X {}^2B_1) + \text{H}^+$  and  $\text{H}_2\text{O}^+(B {}^2B_2) + \text{H}^+$ . The width of the peak around the expected energy of 4.8 eV is evidence for vibrational excitation of both the initial  $\text{H}_3\text{O}^+$  (width toward higher energy) and the formed  $\text{H}_2\text{O}^+$  fragment (width toward lower energy). Initial ionization from the  $1e$  orbital leads mainly to fragmentation into the excited  $\text{H}_2\text{O}^+(B {}^2B_2) + \text{H}^+$  and less intensely to  $\text{H}_2\text{O}^+(A {}^2A_1) + \text{H}^+$ .

For the fragmentation into  $\text{OH} + 2\text{H}^+$ , the relative momentum release distribution of the observed  $\text{H}^+$  fragments is shown in Fig. 10(c). Toward higher momentum releases, the spectrum extends up to  $\sim 0.04$  corresponding to a fragment kinetic energy of  $\sim 9$  eV, which is consistent with fragmentation from  $\text{H}_3\text{O}^+$  with initial  $1e$  ionization fragmenting into  $\text{OH}(X^2\Pi) + 2\text{H}^+$ , considering also a significant vibrational excitation of the intermediate dication. As discussed above, the fragmentations into the channels  $\text{OH}(A {}^2\Sigma^+) + 2\text{H}^+$  after  $1e$  ionization and  $\text{OH}(X^2\Pi) + 2\text{H}^+$  after  $3a_1$  ionization are associated with small momentum releases and a definitive statement on the fragmentation into these channels cannot be made based on the present data.

## B. Relevance

The ground state of the hydronium ion has been experimentally well characterized through spectroscopic measurements (see, e.g., Refs. [8,30]) and was subject to several calculations (see, e.g., [9,10,31]). Excited states of hydronium have also been addressed in selected *ab initio* calculations [27,32] and in electron impact scattering calculations [33]. In the present experiments,  $\text{H}_3\text{O}^+$  is initially ionized to form  $\text{H}_3\text{O}^{2+}$  in a vertical transition, so that potential surfaces of this doubly charged polyatomic species are accessed directly. In comparison to calculations, the observed fragmentation patterns could be used as a sensitive probe of those potential surfaces of  $\text{H}_3\text{O}^{2+}$  accessible in the Franck-Condon region of the well known pyramidal ground state of  $\text{H}_3\text{O}^+$ .

From spectroscopic observations [34], the hydronium ion is known to exist in interstellar gas clouds where it is one of the major oxygen containing species. According to chemical models of these environments [4,5,35],  $\text{H}_3\text{O}^+$  is formed through a sequence of hydrogen additions to  $\text{O}^+$ ,  $\text{OH}^+$ , and  $\text{H}_2\text{O}^+$  through reactions with  $\text{H}_2$  and destroyed by dissocia-

tive recombination with low energy electrons. This is, for instance, the case in the so-called photodissociation or photon dominated regions (PDRs) [4], which exist where neutral interstellar gas clouds are exposed to far ultraviolet radiation (6–13.6 eV) and where the formation of chemically active ions is largely controlled by photoionization and photodissociation. Furthermore,  $\text{H}_3\text{O}^+$  is also formed in x-ray dissociation regions (XDRs) [35–38] that exist where neutral interstellar gas is exposed to x rays and where the thermal and chemical properties are believed to be determined by initial atomic and molecular ionizations. In particular, the impact of x rays on molecules and molecular ions is modeled through inner shell ionization followed by dissociation into singly charged fragments [35,36]. The data presented here on  $\text{H}_3\text{O}^+$  emphasize the photoionization and dissociation reactions in the soft x-ray regime, likely of highest relevance at the interfaces between PDRs and XDRs, by showing that valence shell ionization can be a rather significant process (cross section of  $\sim 10^{-18}$  cm<sup>2</sup>), characterized, however, by only a few active fragmentation channels.

The hydronium ion and in particular higher water hydrate ions  $\text{H}^+(\text{H}_2\text{O})_n$  have been observed in the lower D region of the Earth's ionosphere through direct mass spectrometric measurements [6] and are believed to be formed through a rich chemistry initiated by molecular ionization by high energy solar photons or cosmic rays. The hydronium ion is also believed to be a major ionic component of atmospheres of other planets (e.g., the Martian atmosphere [39,40]) and atmospheres of icy moons of giant planets, for instance, in the Jovian and Saturnian systems [41]. High energy solar radiation may penetrate into the atmospheric regions where  $\text{H}_3\text{O}^+$  exists and the data presented in this paper open the possibility to include, based on laboratory results, hydronium photoabsorption and photofragmentation into chemical models of such atmospheres.

## V. CONCLUSION

We have described an experimental study of the fragmentation patterns of the hydronium cation  $\text{H}_3\text{O}^+$  after absorption of 13.5 nm photons delivered by the Free-electron Laser in Hamburg (FLASH). The data make evident that the photofragmentation of  $\text{H}_3\text{O}^+$  at 13.5 nm is initiated by ionization from a valence shell into  $\text{H}_3\text{O}^{2+}$  which evolves by fragmenting into mainly either  $\text{OH}+2\text{H}^+$  or  $\text{H}_2\text{O}^++\text{H}^+$  with a branching between the two channels of up to 0.6:1. The kinetic energy released in the breakup into  $\text{H}_2\text{O}^++\text{H}^+$  reveals that the emerging molecular fragments are preferentially formed in electronically excited states and most likely also with considerable vibrational excitation. The partial photoabsorption cross section leading to  $\text{OH}+2\text{H}^+$  was found to be  $\sim (0.37 \pm 0.18) \times 10^{-18}$  cm<sup>2</sup>.

The recorded data are consistent with the interpretation that the initial  $\text{H}_3\text{O}^+$  ionization occurs from either the  $3a_1$  or the  $1e$  valence orbital. Starting from the  $3a_1$  orbital, fragmentation was primarily observed into  $\text{H}_2\text{O}^+(A^2A_1)$  whereas for ionization from the  $1e$  orbital, fragmentations into  $\text{H}_2\text{O}^+(B^2B_2)+\text{H}^+$  and  $\text{OH}(X^2\Pi)+2\text{H}^+$  were found to be dominant.

The particular results obtained on  $\text{H}_3\text{O}^+$  can become significant in models of the chemistry of planetary ionospheres, exemplified by the D region of the Earth's ionosphere, where high energy solar radiation penetrates, and for astrophysical gas clouds in the vicinity of hot radiating objects such as massive stars, active galactic nuclei, supernovas, and others.

The experimental system, the TIFF facility dedicated to exploring photon induced fragmentation of molecular ions in the vuv to soft x-ray regime, has been presented in detail. It consists of a crossed-photon-and-ion-beam setup where emerging photofragments are detected on two position and time sensitive detectors allowing for an event based on kinematically complete characterization of the photofragmentation. Since an ion beam is an extremely dilute target the feasibility of the crossed beams experiment relies strongly on the unique photon pulse intensities in the vuv and soft x-ray regime. Following our previous study on  $\text{HeH}^+$  [3], the present work demonstrates that the method of fast beam photofragment momentum imaging combined with intense free-electron laser sources allows to pioneer photolysis in regimes that have not been accessible before, which are, however, of importance for the chemistry of interstellar clouds and planetary ionospheres. Moreover, the results are promising for efficiently probing high lying potential energy curves of more complicated polyatomic ions, in particular considering the fact that the present results were obtained during a 12 h FLASH beam delivery only. With stable operation of the FLASH facility at high photon intensities, also the option of rovibrational cooling through ion trapping could recently be implemented. Motivated by these advances, we are currently developing a new scheme for photoelectron momentum imaging in addition to the fragment imaging system in operation.

## ACKNOWLEDGMENTS

This work has been supported by the Minerva Foundation, the Max-Planck Initiative DESY FEL (MIDFEL), and the Max-Planck Advanced Study Group. H.B.P. acknowledges support from the Lundbeck Foundation. We are greatly indebted to the scientific [2] and technical team at FLASH. We thank H. P. Helm for providing details on the construction of a hollow-cathode ion source.

- [1] V. Ayvazyan *et al.*, *Eur. Phys. J. D* **37**, 297 (2006).
- [2] W. Ackermann *et al.*, *Nat. Photonics* **1**, 336 (2007).
- [3] H. B. Pedersen, S. Altevogt, B. Jordon-Thaden, O. Heber, M. L. Rappaport, D. Schwalm, J. Ullrich, D. Zajfman, R. Treusch, N. Guerassimova, M. Martins, J.-T. Hoefl, M. Wellhöfer, and A. Wolf, *Phys. Rev. Lett.* **98**, 223202 (2007).
- [4] A. Sternberg and A. Dalgarno, *Astrophys. J.* **99**, 565 (1995).
- [5] D. J. Hollenbach and A. G. G. M. Tielens, *Rev. Mod. Phys.* **71**, 173 (1999).
- [6] R. P. Wayne, *Chemistry of Atmospheres*, 3rd ed. (Oxford University Press, New York, 2000).
- [7] T. J. Sears, P. R. Bunker, P. B. Davies, S. A. Johnson, and V. Spirko, *J. Chem. Phys.* **83**, 2676 (1985).
- [8] J. Tang and T. Oka, *J. Mol. Spectrosc.* **196**, 120 (1999).
- [9] A. Miani, A. Beddoni, J. Pesonen, and L. Halonen, *Chem. Phys. Lett.* **363**, 52 (2002).
- [10] X. Huang, S. Carter, and J. Bowman, *J. Chem. Phys.* **118**, 5431 (2003).
- [11] H. Helm and P. C. Cosby, *J. Chem. Phys.* **86**, 6813 (1987).
- [12] D. P. de Briujn, J. Neuteboom, and J. Los, *Chem. Phys.* **85**, 233 (1984).
- [13] D. Zajfman, O. Heber, L. Vejby-Christensen, I. Ben-Itzhak, M. Rappaport, R. Fishman, and M. Dahan, *Phys. Rev. A* **55**, R1577 (1997).
- [14] U. Müller and P. C. Cosby, *J. Chem. Phys.* **105**, 3532 (1996).
- [15] Z. Amitay, D. Zajfman, and P. Forck, *Phys. Rev. A* **50**, 2304 (1994).
- [16] U. Hechtfisher, Z. Amitay, P. Forck, M. Lange, J. Linkemann, M. Schmitt, U. Schramm, D. Schwalm, R. Wester, D. Zajfman, and A. Wolf, *Phys. Rev. Lett.* **80**, 2809 (1998).
- [17] M. Dahan, R. Fishman, O. Heber, M. Rappaport, N. Altstein, W. J. van der Zande, and D. Zajfman, *Rev. Sci. Instrum.* **69**, 76 (1998).
- [18] H. B. Pedersen, D. Strasser, O. Heber, M. L. Rappaport, and D. Zajfman, *Phys. Rev. A* **65**, 042703 (2002).
- [19] H. B. Pedersen, D. Strasser, B. Amarant, O. Heber, M. L. Rappaport, and D. Zajfman, *Phys. Rev. A* **65**, 042704 (2002).
- [20] R. Treusch, HASYLAB Annual Report, 2005 (unpublished), p. 159.
- [21] M. Martins *et al.*, *Rev. Sci. Instrum.* **77**, 115108 (2006).
- [22] RoentDek Handels GmbH, Kelkheim-Ruppertsheim, Germany.
- [23] O. Jagutzki, A. Cerzo, K. Ullmann-Pfleger, L. Spielberger, U. Spillmann, R. Dörner, and H. Schmidt-Böcking, *IEEE Trans. Nucl. Sci.* **49**, 2477 (2002).
- [24] O. Jagutzki, J. Barnstedt, U. Spillmann, L. Spielberger, V. Mergel, K. Ullmann-Pfleger, M. Grewing, and H. Schmidt-Böcking, *Proc. SPIE* **3764**, 61 (1999).
- [25] SIMION, Version 7.0, ion source software.
- [26] R. N. Zare, *Mol. Photochem.* **4**, 1 (1972).
- [27] R. C. Raffanetti, H. J. T. Preston, and J. J. Kaufman, *Chem. Phys. Lett.* **46**, 513 (1977).
- [28] T. Koopmans, *Physica (Amsterdam)* **1**, 104 (1934).
- [29] National Institute of Standards and Technology database, <http://www.nist.gov>.
- [30] T. Furuya, S. Saito, and M. Araki, *J. Chem. Phys.* **127**, 244314 (2007).
- [31] T. Rajamäki, A. Miani, and L. Halonen, *J. Chem. Phys.* **118**, 10929 (2003).
- [32] F. Di Giacomo, F. A. Gianturco, F. Raganelli, and F. Schneider, *J. Chem. Phys.* **101**, 3952 (1994).
- [33] A. Faure and J. Tennyson, *J. Phys. B* **35**, 1865 (2002).
- [34] F. Lovas, *J. Phys. Chem. Ref. Data* **33**, 177 (2004).
- [35] P. R. Maloney, D. J. Hollenbach, and A. G. G. M. Tielens, *Astrophys. J.* **466**, 561 (1996).
- [36] P. Stäuber, S. D. Doty, E. F. van Dishoeck, and A. O. Benz, *Astron. Astrophys.* **440**, 949 (2005).
- [37] R. Meijerink and M. Spaans, *Astron. Astrophys.* **436**, 397 (2005).
- [38] R. Meijerink, M. Spaans, and F. P. Israel, *Astron. Astrophys.* **461**, 793 (2007).
- [39] G. J. Molina-Cuberos, H. Lichtenegger, K. Schwingenschuh, J. J. López-Moreno, and R. Rodrigo, *J. Geophys. Res.* **107**, 5027 (2002).
- [40] S. A. Haider, V. Singh, V. R. Choksi, W. C. Maguire, and M. I. Verigin, *J. Geophys. Res.* **112**, A12309 (2007).
- [41] V. I. Shematovich, *Solar System Research* **42**, 473 (2008).